

Combinatorial Nanopowder Synthesis Along the ZnO–Al₂O₃ Tie Line Using Liquid-Feed Flame Spray Pyrolysis

Min Kim, Samson Lai, and Richard M. Laine[†]

Department of Materials Science and Engineering, University of Michigan, Ann Arbor, MI 48109-2136

Liquid-feed flame spray pyrolysis (LF-FSP) of mixtures of alumatrane [Al(OCH₂CH₂)₃N]/zinc acetate dihydrate [Zn(O₂CCH₃)₂·2(H₂O)] or zinc propionate [Zn(O₂CCH₂CH₃)₂]/aluminum acetylacetonate [Al(Acac)₃] dissolved in EtOH in known molar ratios can be used to combinatorially generate nanopowders along the ZnO–Al₂O₃ tie-line. LF-FSP was used to produce (ZnO)_x(Al₂O₃)_{1-x} powders with $x = 0$ – 1.0 . Powders were characterized by X-ray diffraction, scanning electron microscopy, transmission electron microscopy, Fourier transform infrared, thermal gravimetric analysis, differential thermal analysis, and BET. The resulting powders had average particle sizes (APSS) <100 nm with the majority being <50 nm. Analytical data suggest that at concentrations of interest for transparent conducting oxides, <10 mol% Al₂O₃, the particle morphologies are combinations of plates and rods that grow with c/a ratios close to 1. The spinel phase dominates at (ZnO)_x(Al₂O₃)_{1-x} ($x = 0.5$ and 0.3). In the latter case, the currently accepted phase diagram for the ZnO–Al₂O₃ couple indicates that phase separation should occur to form zinc spinel (ZnAl₂O₄) and α -alumina. It appears that the rapid quenching during LF-FSP helps to preserve the spinel phase at ambient temperature giving rise to kinetic nanopowder products along the ZnO₂–Al₂O₃ tie-line. Finally, the solubility of ZnO in Al₂O₃ and vice versa in the materials produced by LF-FSP suggest apparent flame temperatures reached before quenching are 1700°–1800°C. Efforts to re-pass the spinel phase powders, (ZnO)_x(Al₂O₃)_{1-x}, $x = 0.5$ and 0.3 through the LF-FSP system were made with the hope of generating core shell materials. However, instead the $x = 0.5$ material generated materials closer to the $x = 0.3$ composition and pure ZnO nanoparticles that coat the former materials. These results suggest that at LF-FSP flame temperatures ZnO remains in the vapor phase for sufficient times that Al³⁺ oxygens generated promote nucleation of finer particles leaving essentially phase pure ZnO still in the vapor phase to condense giving the two distinct particle morphologies observed.

I. Introduction

TRANSPARENT conducting oxides or TCOs are used for a wide variety of applications including various display applications as well as photovoltaic, electrochromic, RF shielding, and sensor applications. TCOs typically have band gaps >3.1 eV (absorptions <400 nm) and can have conductivities of $\approx 1 \times 10^4$ S/cm similar to good metal conductors.^{1–10} Although functionally useful TCOs have been made from a wide variety of alloys or doped forms of In₂O₃, SnO₂, Ga₂O₃, ZnO, PbO₂, SbO₂; the commercial material of choice is doped indium oxide,

e.g. In₂O₃:Sn 5–6 at% Sn (ITO). Unfortunately, ITO is expensive because of the scarcity of In. Thus, extensive efforts have been made to find substitutes that provide similar properties at lower costs.

Aluminum-doped zinc oxide or ZnO:Al was first proposed as an ITO substitute by Wasa *et al.* in 1971,¹¹ and has since been the subject of numerous studies, typically in thin films prepared using a variety of deposition methods.^{12–16} One key issue is the thermal stability of ZnO which loses oxygen at temperatures $\geq 150^\circ\text{C}$.¹⁷ In 1984, Minami and colleagues described the preparation of ZnO:Al films stable to $\approx 400^\circ\text{C}$ with resistivities of $\approx 2 \times 10^{-4} \Omega \cdot \text{cm}$.^{8,17,18} ZnO:Al films have recently been used in commercial flat panel displays and thin film solar cells offering resistivities of $1\text{--}3 \times 10^{-4} \Omega \cdot \text{cm}$ at dopant concentrations of 1.6–3.2 at% Al in ZnO.^{8,11–18} Considerable opportunity remains to further modify these materials to improve conductivity, thermal stability, and transparency through further manipulation of both chemical and phase composition as well as processing methods motivate the efforts reported here.⁸

We have previously demonstrated that liquid-feed flame spray pyrolysis (LF-FSP) offers a simple way to produce complex mixed-metal oxide nanopowders.^{19–34} Basically, in the LF-FSP process, alcohol solutions of metalloorganics and occasionally organometallics at 2–10 wt% of ceramic content are aerosolized with oxygen and thereafter ignited. Combustion occurs at temperatures of 1500°–2000°C depending on the precursor, its concentration and processing conditions. Combustion takes place within a 1.5 m quartz tube and the combustion products are quenched at rates of 1000°C/ms. The resulting ceramic soot (metal oxide nanopowders) is collected downstream in electrostatic precipitators. Production rates run 30–100 g/h. The unaggregated and often single crystal nanopowder compositions are the same as those in the original precursor solution. More details are available in the experimental and in previously published papers.^{19–34}

Most recently we demonstrated that LF-FSP processing of MgO-, CuO-, CoO-, ZrO-, CeO-, NiO–Al₂O₃ mixed-metal systems provides access to heretofore unknown and/or unusual spinel phases because of the rapid quench kinetics that occur in the process.^{27–33} Given that some of these materials and phases may offer unique properties inaccessible using standard ceramics processing methods, we sought to extend LF-FSP processing to (ZnO)_x(Al₂O₃)_{1-x} nanopowders hopefully with similar outcomes. The current studies also serve as the basis for LF-FSP processing of (ZnO)_x(Al₂O₃)_{1-x} nanopowders incorporating tertiary and/or quaternary dopants.

It is important to note that there are now two books on the gas phase synthesis of metal oxide nanopowders and a number of reviews including those by several other groups that have explored the use of LF-FSP for the production of nanooxide powders.^{34–41} Although we were unable to identify other groups using LF-FSP to produce Al-doped ZnO, numerous other groups have developed diverse approaches to these materials as mentioned below.

Three phases are found along the ZnO–Al₂O₃ tie-line; ZnO zincite, ZnAl₂O₄ spinel, and α -Al₂O₃ alumina. Based on these

R. Riedel—contributing editor

Manuscript No. 28519. Received August 27, 2010; approved March 27, 2011.

This work was supported by the Air Force Office of Scientific Research, through contracts No. F49620-03-1-0389 and subcontract from UES Inc. F074-009-0041/AF07-T009, Diamond Innovations Inc., the National Science Foundation (IGERT grant DGE-9972776 and DMR 9975542), and Maxit Corp., Oslo, Norway.

[†]Author to whom correspondence should be addressed. e-mail: talsdad@umich.edu

phases, a set of compositions was targeted for LF-FSP processing focusing on two main regions of Al_2O_3 -doped ZnO $[(\text{ZnO})_x(\text{Al}_2\text{O}_3)_{1-x}]$, $x = 0.9\text{--}1.0$] and compositions at the other end of the tie line including the spinel phase region $[(\text{ZnO})_x(\text{Al}_2\text{O}_3)_{1-x}]$, $x = 0.1\text{--}0.5$]. All LF-FSP powders were produced at rates of 30–50 g/h using EtOH as the solvent and fuel. The as-prepared powders were characterized by X-ray diffraction (XRD), transmission electron microscopy (TEM), BET, Fourier transform infrared (FTIR), thermal gravimetric analysis–differential thermal analysis (TGA-DTA), and chemical analysis.

II. Experimental Procedure

(1) Materials

Zinc nitrate $[\text{Zn}(\text{NO}_3)_2 \cdot x(\text{H}_2\text{O})]$, 99% and zinc acetate dihydrate $[(\text{CH}_3\text{COO})_2\text{Zn} \cdot 2\text{H}_2\text{O}]$, 99.9% were purchased from Aldrich (Milwaukee, WI). Triethanolamine $\text{N}(\text{CH}_2\text{CH}_2\text{OH})_3$, anhydrous ethanol $[\text{CH}_3\text{CH}_2\text{OH}]$, 99+%, and methanol were purchased from Alfa Aesar. Aluminum tris (sec-butoxide), $[\text{Al}(\text{OsBu})_3]$, 97% was purchased from Chattem Chemical Co. (Chattam, TN) Aluminum acetylacetonate $[\text{Al}(\text{C}_5\text{H}_7\text{O}_2)_3]$, 99.9% was purchased from Mackenzie Inc. (Bush, LA). All compounds and solvents were used as received.

(2) Precursor Preparation and Pyrolysis

(A) *Zinc Propionate*: $\text{Zn}(\text{O}_2\text{CCH}_2\text{CH}_3)_2$: Zinc nitrate $[\text{Zn}(\text{NO}_3)_2 \cdot x(\text{H}_2\text{O})]$, 99%, 100 g, 0.33 moles] was reacted with excess propionic acid (400 mL, 5.44 mol) in a 1 L flask equipped with a still head and an addition funnel. N_2 was sparged directly through the solution (2 psi pressure) as the solution was heated at $120^\circ\text{C}/2$ h to distill off ~ 150 mL of liquid (water and propionic acid). The resulting solution was slowly heated to distill off excess solvent and reactant. Thereafter the solution was reduced to 100 mL of a viscous green gel by rotary evaporation, and then the gel was dried to a solid under a dynamic vacuum at 70°C . The TGA of this product is discussed in Section III.

(B) *Alumatrane* $[\text{Al}[\text{N}(\text{CH}_2\text{CH}_2\text{O})_3]]$: This was synthesized from $\text{Al}(\text{OsBu})_3$ and $\text{N}(\text{CH}_2\text{CH}_2\text{OH})_3$ as described elsewhere,^{19,22} then diluted with EtOH such that the ceramic yield was 7.5 wt % by TGA.

(C) $(\text{ZnO})_x(\text{Al}_2\text{O}_3)_{1-x}$: A series of precursors corresponding to specific $(\text{ZnO})_x(\text{Al}_2\text{O}_3)_{1-x}$ ($x = 0\text{--}1.0$) powder compositions were prepared. For ZnO-rich composition series, alumatrane was used as the source of Al_2O_3 and methanolic zinc acetate solutions for ZnO. For the remaining ZnO– Al_2O_3 tie-line compositions, we used aluminum acetylacetonate $[\text{Al}(\text{Acac})_3]$ as the source of Al_2O_3 and $\text{Zn}(\text{O}_2\text{CCH}_2\text{CH}_3)_2$ for ZnO, because zinc acetate is only slightly soluble in EtOH.

Measured volumes of the two solutions, based on the molar ratio of Zn and Al, were mixed in the appropriate amounts to make 500 mL solutions for each precursor compositions listed in Table I Section III, and then 2.5 L of EtOH was added to give a final volume of 3000 mL with stirring at room temperature.

(3) LF-FSP

LF-FSP, as developed at the University of Michigan, has been described in detail in published papers.^{19–33,42} Briefly, alcohol (typically EtOH) solutions containing 1–10 wt % loading of ceramic as precursors, e.g. single- or mixed-metal alkoxides, carboxylates or β -diketonates are aerosolized with O_2 into a 1.5 m quartz chamber where it is ignited with methane pilot torches.

Initial combustion temperatures run $1500^\circ\text{--}2000^\circ\text{C}$, depending on the processing conditions, generating nanopowder “soot.” Gas phase temperatures in the flame were measured using a two-color Omega S3753 optical pyrometer (Omega Engineering Inc., Stamford, CT) (calibrated using 304 steel T_m and an external thermocouple) used in peak mode (recording at highest temperature in the flame).

Temperatures decline to $300^\circ\text{--}500^\circ\text{C}$ over 1.5 m, equivalent to a 1000°C quench in ≤ 100 ms leading to kinetic products and

nanopowders that are largely unaggregated; although they are lightly agglomerated. “Shooting” rates can be 200 g/h when using wire-in-tube electrostatic precipitators operating at 10 kV. Typical powders are 15–100 nm APS with specific surface areas (SSAs) of 30–100 m^2/g . When combinations of elements are used, the resulting nanopowders will have compositions identical to those of the precursor solutions. Because compositions of chemical solutions can be changed intentionally, potentially even during mixing just before aerosolization, it becomes possible to combinatorially produce mixed-metal oxide materials. Hence it becomes possible to rapidly optimize materials for given properties or for ease of processing.

(4) Characterization

(A) *TGA/DTA*: Phase transformations and mass loss events occurring during heating of as-prepared samples were investigated via simultaneous differential thermal (SDT) analyzer (TA Instruments Inc., New Castle, DE). The transformation temperatures determined by TGA were also done using a model 2960 simultaneous thermogravimetric analyzer (TA Instruments, Newcastle, DE).

As-prepared powders of about 20 mg were hand pressed in a 3 mm dual action die and placed inside Pt sample cups and heated at ramp rates of $10^\circ\text{C}/\text{min}$ from room temperature to 1400°C . The reference material was a pellet of α -alumina. A synthetic air flow of 50 mL/min was maintained during all SDT experiments. Precursor samples were placed in alumina sample cups with an empty alumina cup as the reference and heated at ramp rates of $10^\circ\text{C}/\text{min}$ up to 1000°C .

(B) *XRD*: As-prepared and heat-treated (air/nitrogen) samples were characterized using a Rigaku Rotating Anode Goniometer (Rigaku Americas, The Woodlands, TX). Powder samples for the Rigaku were prepared by placing ≈ 100 mg in XRD sample holders (amorphous silica slides) for data collection. $\text{CuK}\alpha$ ($\lambda = 1.54$ Å) radiation with a Ni filter was used with a working voltage and current of 40 kV and 100 mA, respectively. Scans were continuous from 10° to $80^\circ 2\theta$ with a step scan of $2^\circ 2\theta/\text{min}$ and increments of $0.05^\circ 2\theta$. Peak positions and relative intensities were characterized by comparison with PDF files for zincite (ZnO), normal spinel (ZnAl_2O_4), nonstoichiometry spinel $[(\text{Zn}_{0.3}\text{Al}_{0.7})\text{Al}_{1.7}\text{O}_4]$, and δ - Al_2O_3 , (36-1451), (05-0669), (77-0732), and (42-1215), respectively.

(C) *SSA*: SSA was measured on a Micromeritics ASAP 2000 sorption analyzer (Micromeritics Instrument Corporation, Norcross, GA). Samples (200 mg) were degassed at 400°C until the outgas rate was 5 mmHg/min. Analyses were run at 77 K with N_2 . SSAs were determined by the BET multipoint method using at least five data points with relative pressures of 0.001–0.20. The average particle size (APS) was derived using the formula $\langle D \rangle = \frac{6}{\rho \times \text{SSA}}$ where $\langle D \rangle = \text{APS}$, and ρ is the density of the material.

Table I. Selected $(\text{ZnO})_x(\text{Al}_2\text{O}_3)_{1-x}$ Nanopowder Compositions Produced by Liquid-Feed Flame Spray Pyrolysis (LF-FSP)

Sample	Mol% of Al_2O_3	Mol% of ZnO
From zinc acetate and alumatrane		
95 mol% ZnO	5	95
97.5 mol% ZnO	2.5	97.5
99 mol% ZnO	1	99
99.5 mol% ZnO	0.5	99.5
99.8 mol% ZnO	0.3	99.8
100 mol% ZnO	0	100
From zinc propionate and aluminum acetylacetonate		
10 mol% ZnO	90	10
30 mol% ZnO	70	30
50 mol% ZnO	50	50
80 mol% ZnO	20	80
95 mol% ZnO	5	95
99 mol% ZnO	1	99

(D) *TEM*: An analytical high-resolution TEM (Model 3011, JEOL, Osaka, Japan) was used to measure the particle sizes and morphologies of as-prepared powders. Powder samples were prepared by dipping a holey carbon grid in a vial of emulsion with as-prepared powder. The specimen was held in a Gatan double tilt goniometer (Gatan Inc., Pleasanton, CA). An operating voltage of 300 kV was used.

(E) *Scanning Electron Microscopy (SEM)*: A high-resolution SEM (FEI NOVA dual beam-focused ion beam workstation and scanning electron microscope) was used to image powder morphologies. Powder samples were dispersed in distilled H₂O using an ultrasonic horn (Vibra-cell, Sonics and Materials Inc., Newton, CT). A drop of the dispersed powder/water was placed on an aluminum SEM stub and allowed to dry for 4 h on a hot plate. Powders were sputter coated with 1–5 nm of Au–Pd to reduce charging effects. The operating voltage was 15.0 kV.

III. Results and Discussion

The objectives of the current study were to develop structure–property–processing parameters for LF-FSP production of (ZnO)_x(Al₂O₃)_{1–x} oxide nanopowders along the ZnO–Al₂O₃ tie line including spinel (ZnAl₂O₄) composition regions as listed in Table I. Details of the LF-FSP process are given in Section II. The first step in processing nanopowders by LF-FSP is in the choice of a precursor. The following section briefly explores the issues with precursor choice.

(1) Precursor Choices

A wide variety of precursors have been used in the fabrication of (ZnO)_x(Al₂O₃)_{1–x} nanopowders, coatings, and nanowires. These include metalloorganics such as carboxylates, acetylacetonates and alkoxides,^{43–51} organometallics such as diethylzinc and trimethylaluminum^{52–54} and simple nitrates and sulfates.^{51,55–57} Alternate processing approaches use simple sputtering of targets preformed from powders or direct oxidation of zinc metal or its oxide in flowing gas.^{56,58}

Metal carboxylates, acetylacetonates, and alkoxides are often chosen as precursors for processing metal oxide materials as an alternative to metal halides, nitrates, and sulfates in an effort to avoid halide and sulfate contamination of the resulting oxides. Nitrates typically offer excellent solubility in water and polar solvents but often generate copious amounts of NO_x gases during processing that present significant handling drawbacks. Metal alkyls are very reactive and flammable and as such not easily handled in a typical ceramics processing laboratory.

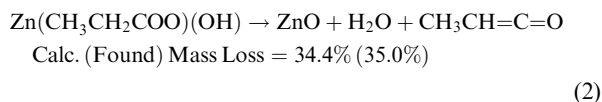
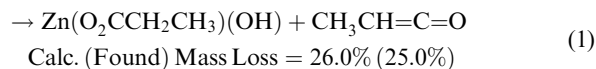
Of the metalloorganic precursors, metal acetylacetonates are very useful for vapor processing of thin films and coatings but are often not as polar as carboxylates or alkoxides and therefore not as soluble [e.g. Al(Acac)₃] in polar solvents such as alcohols often used in sol–gel processing and or spray and flame spray pyrolysis systems. Indeed, the simplest metal carboxylates such as Zn(OAc)₂ are not easily dissolved in alcohols. Thus from a solubility aspect, the simplest, lowest cost, and easily prepared carboxylates are the propionates. We have reported that triethanolamine complexes of transition metals (trane complexes) are relatively insensitive to hydrolysis compared with most alkoxides and as such offer a simple alternative to most aluminum alkoxide precursors.^{22,26}

Thus, we originally developed precursor systems based on Zn(OAc)₂ and Al(OCH₂CH₂)₃N (alumatrane).²² However, during the course of these studies we replaced Zn(OAc)₂ with Zn(O₂CCH₂CH₃)₂ finding it more soluble and more easily handled and alumatrane with Al(Acac)₃ although its solubility is limited. Thus, most of our LF-FSP precursor solutions were made at low total concentrations of precursors.

We previously reported the characterization of alumatrane [N(CH₂CH₂O)₃Al] and its use as a precursor in LF-FSP for the synthesis of δ-alumina nanopowders.^{22,24,29–33,59} Here we report on the zirconium precursor, Zn(O₂CCH₂CH₃)₂ synthesized as discussed in the Section II. This precursor has a thermal de-

composition pattern similar to other metal carboxylate precursors studied previously.^{29–33}

Figure 1 shows a TGA trace for Zn(O₂CCH₂CH₃)₂. Initial mass losses (2%) are due to propionic acid of recrystallization. Thereafter, mass loss events are attributed to the decomposition of the propionate ligands as reaction suggested in reactions (1) and (2).^{22,24,29–33}



Final ceramic yields [37 wt% (ZnO)] are within experimental error of the calculated value (37.6 %) from the decomposition of the precursor [Zn(O₂CCH₂CH₃)₂] to the oxide (ZnO) and are as expected based on previous studies.^{22,24,29–33}

(2) LF-FSP Processing Conditions

As we have described in previous publications, our LF-FSP processing conditions typically involve aerosolizing ethanol solutions of soluble precursors in the desired stoichiometric ratios with oxygen. The resulting aerosol is ignited using methane/O₂ pilot torches inside a 1.5 m by 30-cm-diameter quartz tube. Combustion occurs at temperatures of 1500–2000°C followed by rapid quenching to temperatures near 400°C at the end of the quartz tube. The resulting powders are captured in electrostatic precipitators thereafter and collected by hand. Rates of production are typically 10–20 g/h but can be effected at up to 200 g/h as desired. Gas phase temperatures in the flame were measured using an optical pyrometer. However, these temperatures are reaction system dependent and thus a range of temperatures is given.

LF-FSP processing allows the use of mixed-metal precursors, mutually soluble in alcohol, of any composition to be aerosolized and combusted. Therefore, LF-FSP offers access to high SSA nanopowders consisting of single-phase, solid solutions and mixed-phase nanopowders in the (ZnO)_x(Al₂O₃)_{1–x} oxide system.

As noted above, several other groups also conduct gas phase processing including spray pyrolysis and flame spray pyrolysis. In these systems, the typical flame temperatures are closer to 1000°C; although in several recent reviews temperatures as high as 3000°C are discussed.^{40–42} These latter temperatures are more akin to those of plasma processing.

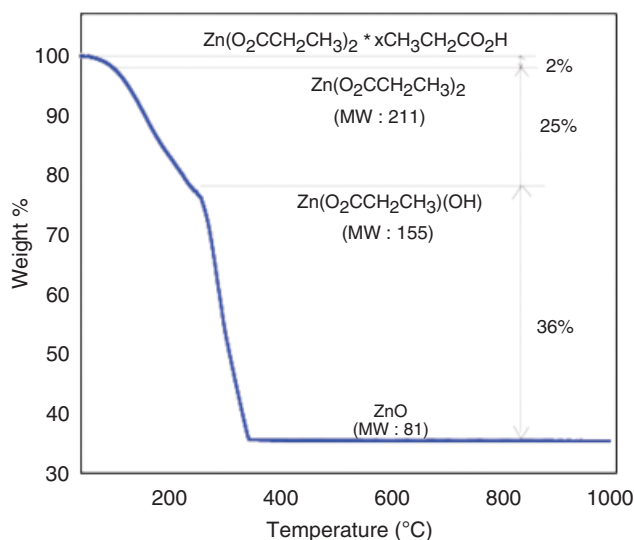


Fig. 1. TGA of Zn(O₂CCH₂CH₃)₂ ramped at 10°C/min in synthetic air. Note the 2 wt% mass loss results from propionic acid or waters of crystallization.

In general, LF-FSP processing as practiced at UM differs considerably from other groups because we work with turbulent flames rather than laminar flow systems. Furthermore, in addition to having somewhat higher temperatures, our precursor throughput is much higher than other researchers who often produce milligrams/hour. These differences appear to lead to quite different products in some instances.

(3) Power Processing Studies

Below, we first discuss what is known about the ZnO–Al₂O₃ phase diagram, and then discuss the types of powders made and their specific characteristics.

The ZnO–Al₂O₃ phase diagram was first described by Bunting⁶⁰ in 1932 but does not incorporate ZnO:Al solid solutions (up to 5 mol% Al₂O₃ depending on the synthesis temperature) and off-stoichiometric spinel phases. Hansson *et al.*⁶¹ recently revised the phase diagram, adding two solid solution regions to Bunting’s work. First, the maximum solubility of Al₂O₃ in zincite was found to be 4.7 mol% at 1695°C and was found to decrease rapidly with decreasing temperatures to ≤0.5 mol% at 1550°C and below. The spinel composition is reported as the mineral gahnite (ZnAl₂O₄) when Al₂O₃ is in equilibrium with zincite ZnO.³⁶

LF-FSP flame synthesis occurs at temperatures of 1500°–2000°C, thus we are potentially able to explore the solubility limit of Al in ZnO at much higher temperatures than possible for standard ceramics processing methods and by virtue of the rapid quenching that occurs in LF-FSP, produce powders with relatively extreme compositions, e.g. at the edge of the currently known solubility limits.

However, nanopowders produced by LF-FSP show higher solubility (up to 20 mol% Al₂O₃) at ZnO-rich compositions than the phase diagram.³⁶ As with many of our previous studies, LF-FSP materials generated by rapid quenching lead to novel kinetic products not expected based on traditional processing methods. Since traditional processing methods lead to thermodynamically rather than kinetically defined phase compositions, these materials may offer unique opportunities for a wide variety of application including various display applications and/or photovoltaic, electrochromic, RF shielding, and sensor applications.

(4) Compositions

The set of compositions listed in Table I were produced using LF-FSP. First, we made ZnO-rich compositions from zinc acetate and alumatrane, then the overall composition series with zinc propionate and aluminum acetylacetonate.

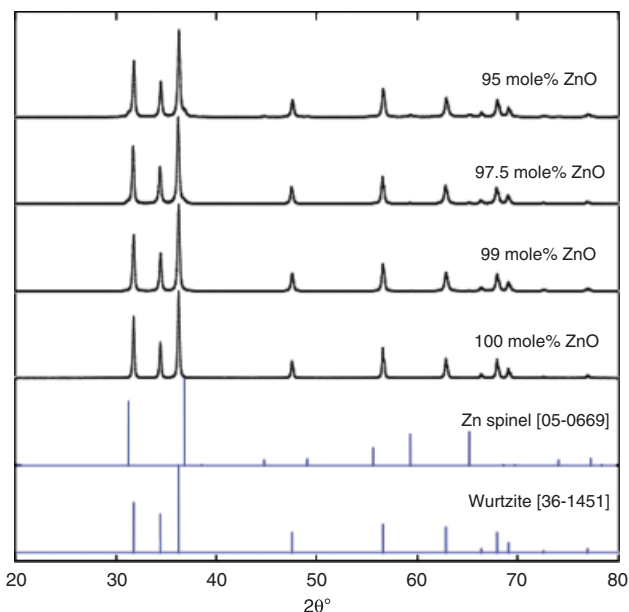


Fig. 2. XRD patterns of (ZnO)_x(Al₂O₃)_{1-x} nanopowders from zinc acetate and alumatrane.

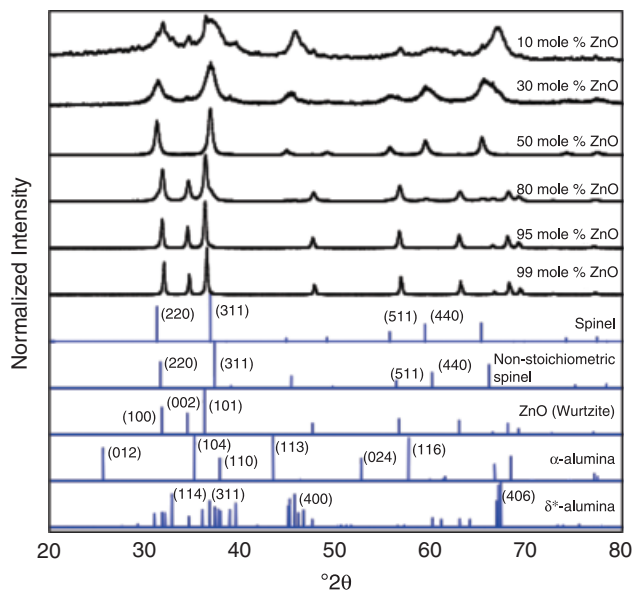


Fig. 3. XRD powder patterns of as-processed (ZnO)_x(Al₂O₃)_{1-x} nanopowders by LF-FSP wurtzite ZnO (PDF file: 36-1451), spinel ZnAl₂O₄ (PDF file: 05-0669), nonstoichiometric spinel (Zn_{0.3}Al_{0.7})Al_{1.7}O₄ (PDF file: 77-0732), α-alumina (PDF file: 71-1124), δ*-Al₂O₃ (PDF file: 46-1215).

(5) XRD Studies

Here we begin with the ZnO-rich samples from zinc acetate and alumatrane, which form Al-doped zincite nanopowders. The XRDs for the majority of the compositions are given in Fig. 2. 100 mol% ZnO (pure ZnO) has the hexagonal wurtzite structure in accord with PDF [36-1451]. The XRDs of the 95–100 mol ZnO compositions show that hexagonal zincite is the major phase. However, a very small (440) peak at 65.2° 2θ seen in the XRD supports spinel phase formation for compositions 97.5 and 95 mol% ZnO.

Because of solubility issues with zinc acetate, we switched to zinc propionate Zn(O₂CCH₂CH₃)₂ for the broader set of compositions including the spinel phase region. We also switched to aluminum acetylacetonate [Al(Acac)₃] from alumatrane. Figure 3 provides XRD patterns for all as-produced nanopowders along the (ZnO)_x(Al₂O₃)_{1-x} tie-line.

In Fig. 3, the Zn-rich samples (99, 95 mol% ZnO) show only wurtzite (PDF 36-1451) suggesting improved miscibility for this precursor system. For 80 mol% ZnO, wurtzite is the main phase, but traces of spinel ZnAl₂O₄ are also observed as a weak (440) peak appears at 65.2° 2θ supporting spinel phase formation.

For samples with 30 and 50 mol% ZnO, ZnAl₂O₄ spinel is observed as the main phase. The formation of 100% spinel phase at 50 mol% ZnO is expected.³⁶ However, the 30 mol%

Table II. Particle Sizes (nm) Measured by FWHM of XRD and the Aspect Ratios (c/a)

(hkl)	100 mol% ZnO	99.8 mol% ZnO	99 mol% ZnO	97.5 mol% ZnO	95 mol% ZnO
(100)	134	68	44	39	33
(002)	150	59	41	32	34
(101)	114	54	38	32	29
(102)	100	47	34	30	31
(110)	101	55	36	32	32
(103)	90	41	28	27	27
(112)	88	47	31	27	29
(201)	88	51	34	33	29
Aspect ratio (c/a)	1.12	0.87	0.93	0.82	1.03

Table III. Lattice Parameters Measured by X-Ray Diffraction Using (100) and (101) Peaks

	100 mol% ZnO	99.8 mol% ZnO	99 mol% ZnO	97.5 mol% ZnO	95 mol% ZnO
<i>a</i>	3.2442	3.2506	3.2508	3.2532	3.2490
<i>c</i>	5.1900	5.2084	5.2068	5.2128	5.2022
Cell volume	94.6	95.3	95.3	95.6	95.1

ZnO sample is also almost phase pure spinel in contrast to existing thermodynamic data where phase separation between spinel and α -alumina should be found. In the phase diagram, phase pure spinel with a 30 mol% ZnO composition forms only between 1700° and 1800°C. One could argue that in LF-FSP, phase pure spinel forms and the spinel structure is preserved by rapid quenching to ambient temperature, forming a kinetic product.

Thus, we can suggest that the effective LF-FSP operating temperature is 1700°–1800°C. The term “effective” is used because we are not able to estimate the effect(s) of the very small particle sizes and therefore high surface energies on the solubility of one oxide phase in the other.

The 10 mol% ZnO sample shows phase separation between spinel and δ -alumina; different from the phase diagram where phase separation should lead to spinel and α -alumina. According to Hinklin *et al.*,²² the formation of δ -alumina might be favored during LF-FSP processing. One can argue that kinetic transition alumina formed during LF-FSP is unable to transform to the thermodynamically stable α -alumina, because of

Table IV. Average Particle Sizes and Specific Surface Areas of $(\text{ZnO})_x(\text{Al}_2\text{O}_3)_{1-x}$ Nanopowders

Sample ZnO (mol %)	Particle size (nm)		
	XRD line broadening	BET-derived	SSA (m ² /g)
99	16	36	30
95	14	32	33
80	13	30	39
50	13	26	50
30	12	22	59
10	12	22	63

rapid quenching (1000°C/ms). A detailed discussion of the formation of transition aluminas rather than α -Al₂O₃ at these temperatures is presented elsewhere.⁵⁹

(6) APSs and SSAs from BET

Table II provides APSs of samples from zinc acetate and alumatrane along the different plane directions as measured using Debye-Scherrer methods. 100 mol% ZnO (pure ZnO) has the largest APSs of 90–150 nm depending on the crystallographic plane.

Crystallite sizes decrease to ~30 nm for 95 mol% ZnO. XRDs of the (*hkl*) 100, 002, and 101 reflections of all LF-FSP prepared samples showed no evidence of preferred growth orientations in contrast to reports for sputtered materials with even less Al doping.¹³

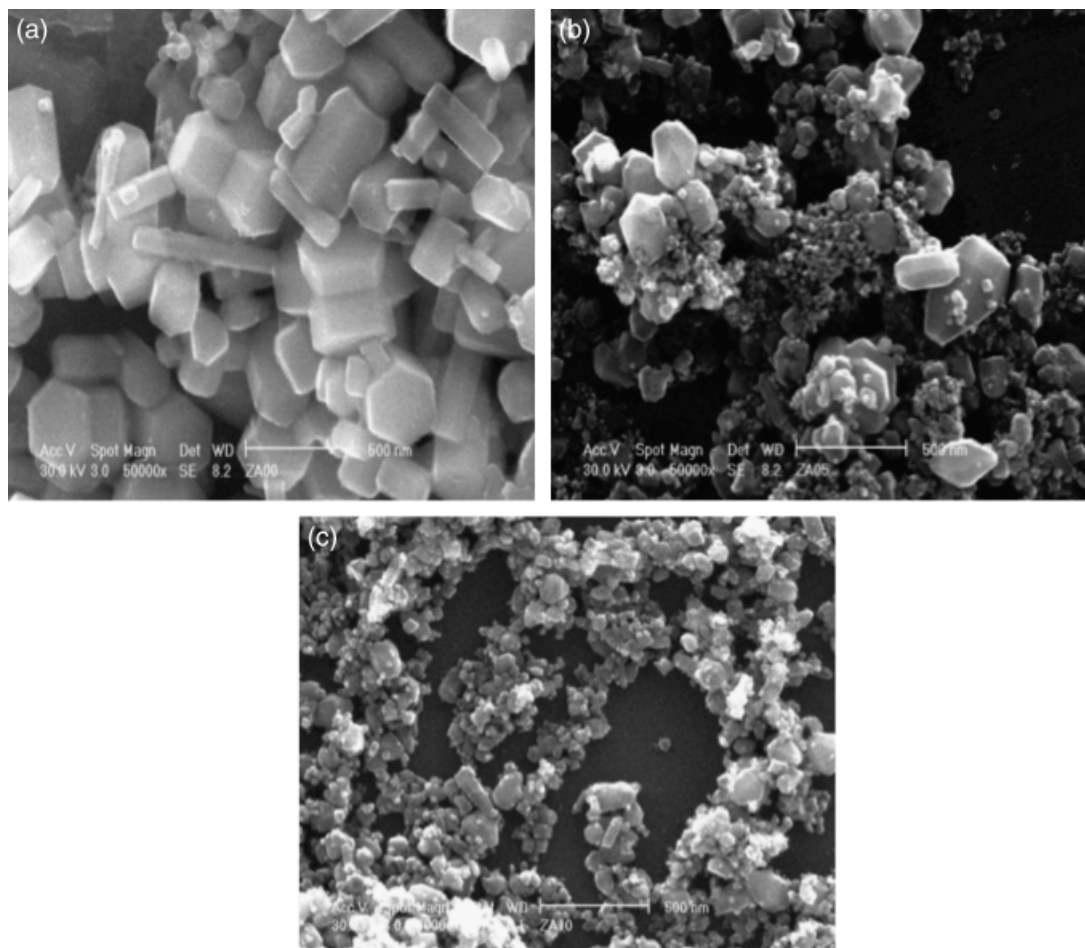


Fig. 4. SEM micrographs of as-prepared nanopowders made from zinc acetate and alumatrane. (a) 100, (b) 97.5, and (c) 95 mol% ZnO samples.

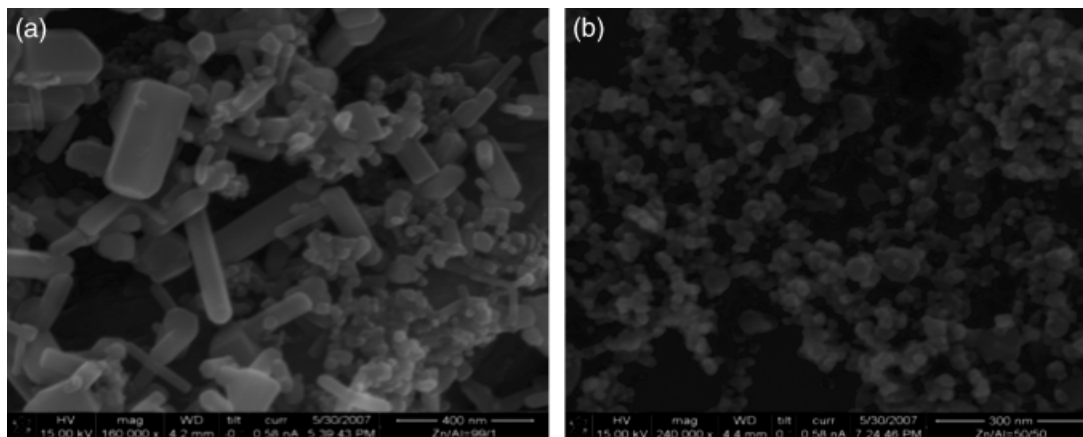


Fig. 5. SEM images of (a) 99 mol% ZnO with Al_2O_3 ; (b) 50 mol% ZnO in Al_2O_3 .

Lattice parameters determined using the (100) and (101) peaks (Fig. 2) show c/a axis ratios of <2.0 as listed in Table III. In Table III, it can be seen that the d -spacings of both the a - and c -axes increase when the amount of Al^{3+} increases indicating that the cell volume increase is proportional to the Al^{3+} ion concentrations. Note that these values are the averages gleaned from XRD data and may average in data for pure ZnO with data for nanoparticles that have somewhat higher Al^{3+} concentrations based on the arguments made below concerning the mechanisms for particle formation.

Since the Al^{3+} radius (0.053 nm) is smaller than that of Zn^{2+} (0.075 nm), the expansion of the lattice constants in both directions might be explained in terms of the incorporation of Al^{3+} ions in interstitial sites as has been suggested by other authors,^{62,63} not by substitution of Zn^{2+} by Al^{3+} . If Al^{3+} ions were to substitute for Zn^{2+} , one would expect that the total cell

volume decrease. However, the 95 mol% ZnO cell volume is lower than that for 99.8 mol% ZnO, which indicates that the concentration of Al ions is above the solubility limit in ZnO at this composition (maximum is 4.7 mol% per Hansson *et al.*).⁶⁴ The maximum cell volume is found for 97.5 mol% ZnO. For 99.8, 99.0, and 97.5 ZnO mol% compositions, our results suggest that Al^{3+} dissolves in ZnO, likely due to the rapid quenching during the LF-FSP process. Unfortunately, the exact explanation for these observations is beyond the scope of this paper.

The APSs for samples from zinc propionate and aluminum acetylacetonate were estimated from Debye-Scherrer line broadening and their SSAs (Table IV). The BET particle sizes are about twice the Debye-Scherrer APSs perhaps because some necking occurs between single crystal particles. This would lead to lower surface areas than expected and reduced APSs.

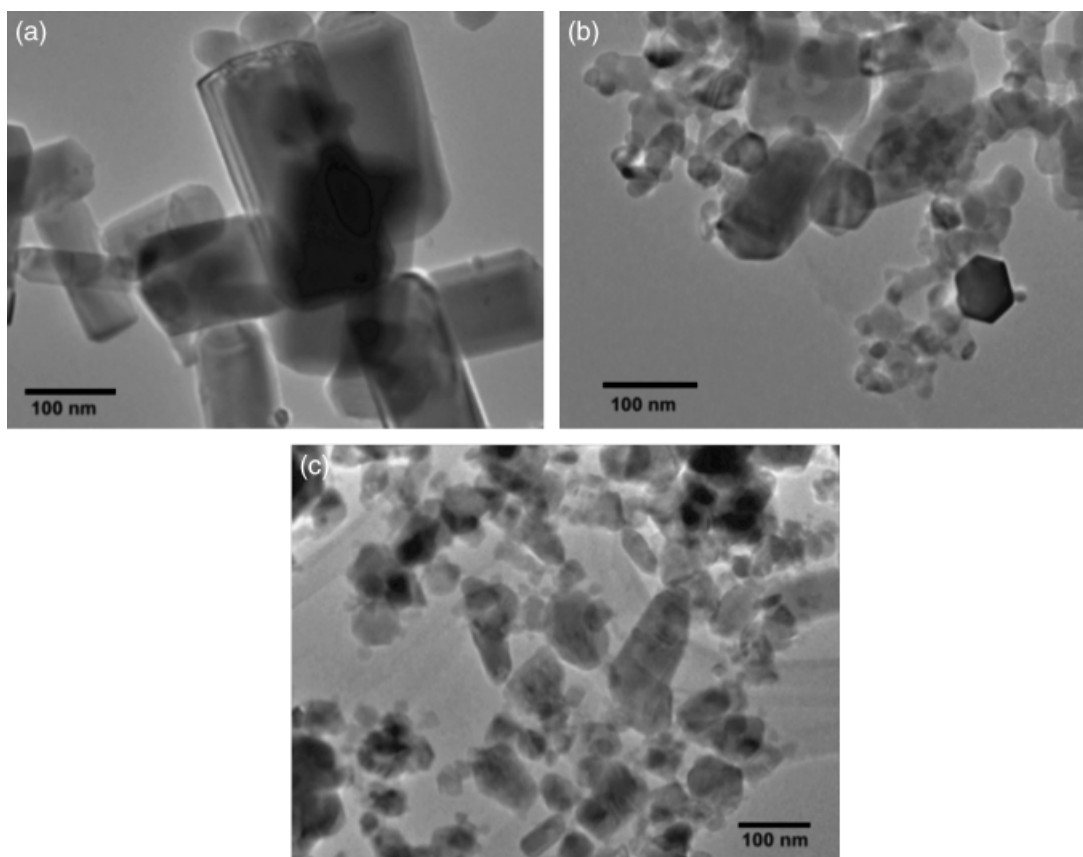


Fig. 6. TEM micrographs of as-prepared powders: (a) 100, (b) 99.8, and (c) 95 mol% ZnO.

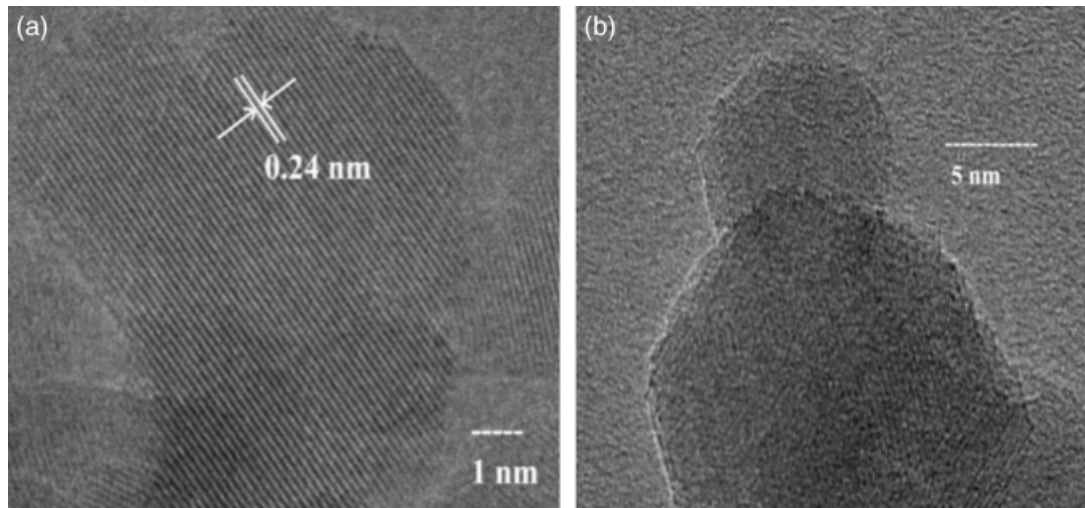


Fig. 7. TEM images of (a) 50 mol% ZnO in Al_2O_3 ; (b) 30 mol% ZnO in Al_2O_3 .

(7) SEM and TEM

High-resolution microscopy was used to assess particle morphologies as a function of chemical and phase composition. SEMs of the 100, 97.5, and 95 mol% ZnO samples made from zinc acetate and alumatrane are shown in Fig. 4. Pure ZnO (ZA00) powders consist of hexagonal rods and platelets. The addition of small amounts of alumina in the 97.5 and 95 mol% ZnO powders results in significant reductions in APSs from the pure ZnO powders. Similar reductions in particle size on increasing Al^{3+} content have been observed before.⁴⁵ This APS reduction in the SEM images matches with the APS data from XRD line broadening in previous section. However, particles > 100 nm are still seen in both samples.

SEM was also used to demonstrate powder uniformity for the samples from zinc propionate and aluminum acetylacetonate. Figure 5 shows that SEM resolution is insufficient to reveal individual particles but does provide a view of the general particle population.

For a ZnO-rich sample (Fig. 5(a)) shows dominant cylindrical-shaped particles with irregular c/a ratios, and a bimodal distribution of APSs. For a spinel region sample (Fig. 5(b)), most particles are spherical and APSs are less than 50 nm. These SEMs indicate that the particle populations produced here do not include any obvious micrometer size particles.

TEM micrographs of 100, 99.8, and 95 mol% ZnO samples are shown in Fig. 6. While small particles (< 15 nm in particle sizes) are not observed in pure ZnO powders, the 99.8 mol% ZnO powders show significant amounts of fine particles with APSs < 30 nm compared with the pure ZnO powders.

The increase in number of small sized particles in 99.8 and 95 mol% ZnO samples also matches with XRD line broadening results and SEM images. It appears that there is a bimodal size distribution at 25 and 250 nm in these powders, while the compositions close to the spinel region show more uniform and smaller APSs.

The morphologies also change with Al^{3+} doping. As the amount of Al increases, the resulting particles tend toward rods indicating enhanced growth along the c -axis perhaps indicating somewhat selective addition of Al^{3+} ions to one growth face. However, detailed studies show that correlate particle size and shape as a function of Al^{3+} content were not pursued further.

TEM images were also used to gather information on particle morphologies and sizes of as-prepared powders at the spinel composition. Discussions of actual size/size distributions are not appropriate if based solely on TEM micrographs, unless combined with the XRD results and SEM images. Figure 7 offers high-resolution TEM images of $(\text{ZnO})_x(\text{Al}_2\text{O}_3)_{1-x}$ nanopowders

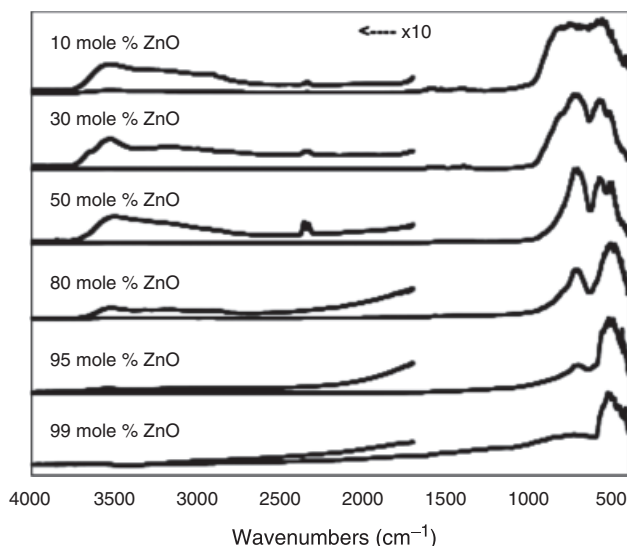


Fig. 8. DRIFTs of as-processed $(\text{ZnO})_x(\text{Al}_2\text{O}_3)_{1-x}$ nanopowders.

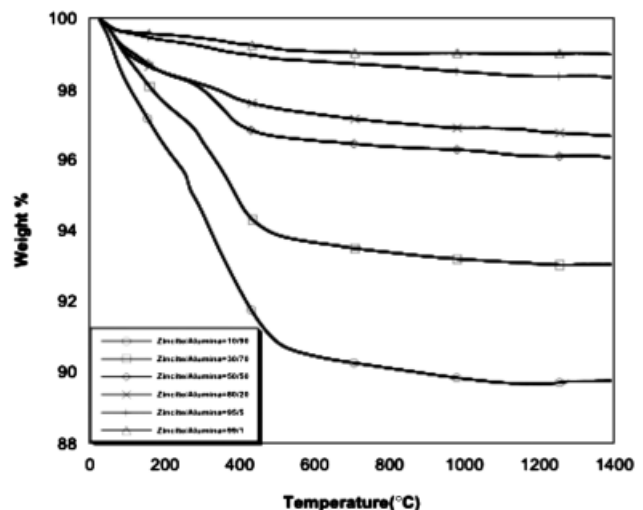


Fig. 9. TGAs of as-processed $(\text{ZnO})_x(\text{Al}_2\text{O}_3)_{1-x}$ nanopowders made from zinc propionate and aluminum acetylacetonate ($10^\circ\text{C}/\text{min}$, in air).

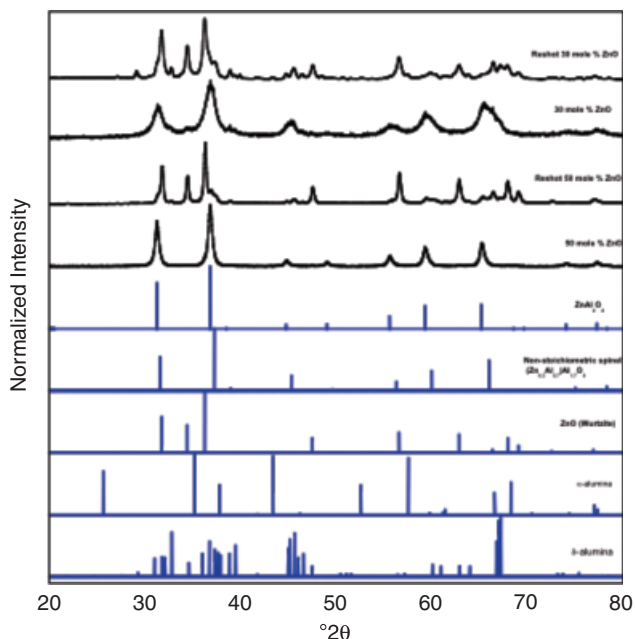


Fig. 10. XRDs of as-prepared and reprocessed nanopowders of spinel composition.

from LF-FSP. Particle sizes here are typically <30 nm in diameter with the vast majority <20 nm. Figure 7(a) shows clear unidirectional lattice planes, [$d=2.4$ Å for (311) planes, cubic spinel phase]. The d -spacing values from TEM images confirm our XRD results concerning spinel phase at 50 mol% ZnO composition. Multifaceted single particles are likely a consequence of particle formation during rapid quench from the gas phase.

(8) Diffuse Reflectance Infrared Fourier Transform Spectroscopy

Once the particle morphologies were characterized by XRD and high-resolution microscopy, the particle surface chemistries were characterized using FTIR. DRIFT spectra for $(\text{ZnO})_x(\text{Al}_2\text{O}_3)_{1-x}$ nanopowders are presented in Fig. 8. Higher wavenumber (>1500 cm^{-1}) regions were first normalized and then multiplied $10\times$ in an effort to observe $\nu\text{C-H}$ or $\nu\text{O-H}$ bands on

powder surfaces. These spectra offer little evidence for either $\nu\text{C-H}$ or $\nu\text{O-H}$ bands.

The as-processed nanopowders have no significant organic species on the surface, as the absence at $2900\text{--}2700$ cm^{-1} $\nu\text{C-H}$ vibrations suggests.⁶⁵ $\nu\text{O-H}$ vibrations ($3800\text{--}3200$ cm^{-1}) show both chemi- and physisorbed water on the surface of nanopowders.⁶⁶

$\nu\text{M-O}$ bands are observed in the $1200\text{--}400$ cm^{-1} region. The spinel structure (80, 50, and 30 mol% ZnO) is confirmed by FTIR spectra, as there are three characteristic peaks at 510, 570, and 690 cm^{-1} corresponding to a normal spinel structure with octahedrally coordinated Al^{3+} .^{67,68} The bands at $450\text{--}600$ cm^{-1} show $\nu\text{Zn-O}$ bands typical of the wurtzite structure, which dominate Zn-rich samples (95, 99, 80 mol% ZnO).^{69,70}

(9) TGA-DTA Studies

TGAs were performed in air on all as-prepared powder samples to determine the relative amounts of surface species and thermal behavior. The thermal stability of the powders was investigated using DTA. Figure 9 shows the TGA for the series of powders. The DTAs are not shown, because they are not informative, no phase transformations are observed.

All as-processed powders exhibit 0.5–5.0 wt% mass losses up to $\approx 300^\circ\text{C}$, typical of LF-FSP produced nanopowders that can be attributed to evolution of both physi- and chemisorbed water as seen in the FTIR (Fig. 8).⁶⁶ Mass losses between 300° and 400°C are due to elimination of carbonate species as CO_2 . The amount of mass loss is proportional to the amount of alumina as seen previously.^{29–33}

(10) Reprocessing Spinel Composition Nanopowders by LF-FSP

We recently re-shot δ -alumina using LF-FSP causing δ -alumina transform to α -alumina.⁵⁹ Based on this result, we realized that given that 30 mol% ZnO composition gives pure nonstoichiometric spinel phase (PDF file: 77-0732) as a kinetic product, we might expect core-shell nanostructured nanoparticles to form with spinel and α -alumina using LF-FSP reprocessing based on the phase diagram thermodynamic data and the nucleation differences between spinel and α -alumina due to different boiling/melting points.^{32–42,59} Therefore, we re-shot as-produced spinel composition nanopowders (30 and 50 mol% ZnO), because we anticipated that the as-processed spinel nanoparticles might phase separate to spinel and α -alumina during reprocessing. The existing phase diagram suggests that phase separation

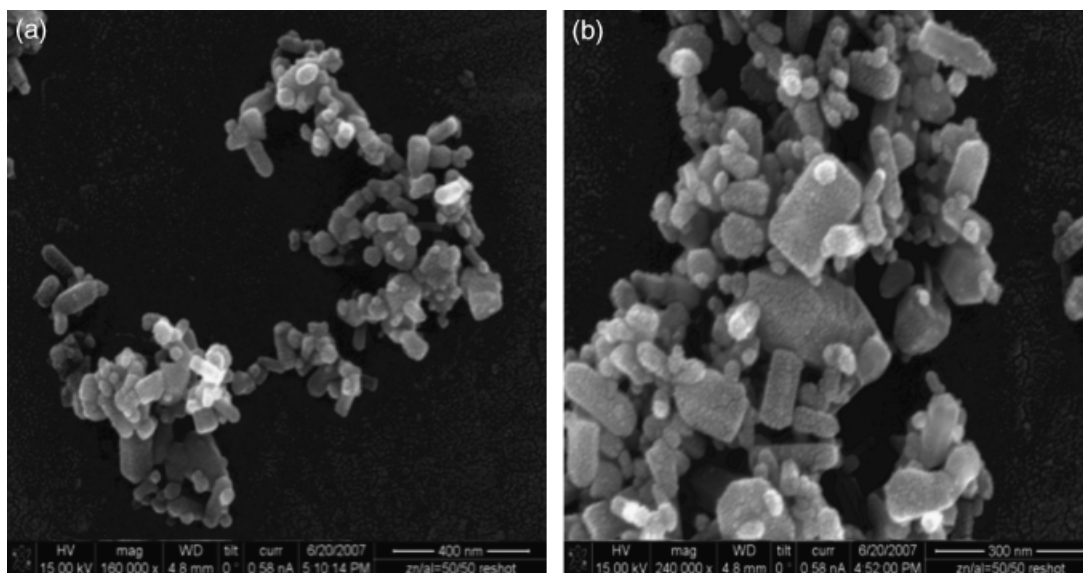


Fig. 11. SEM images of re-shot 50 mol% ZnO in Al_2O_3 .

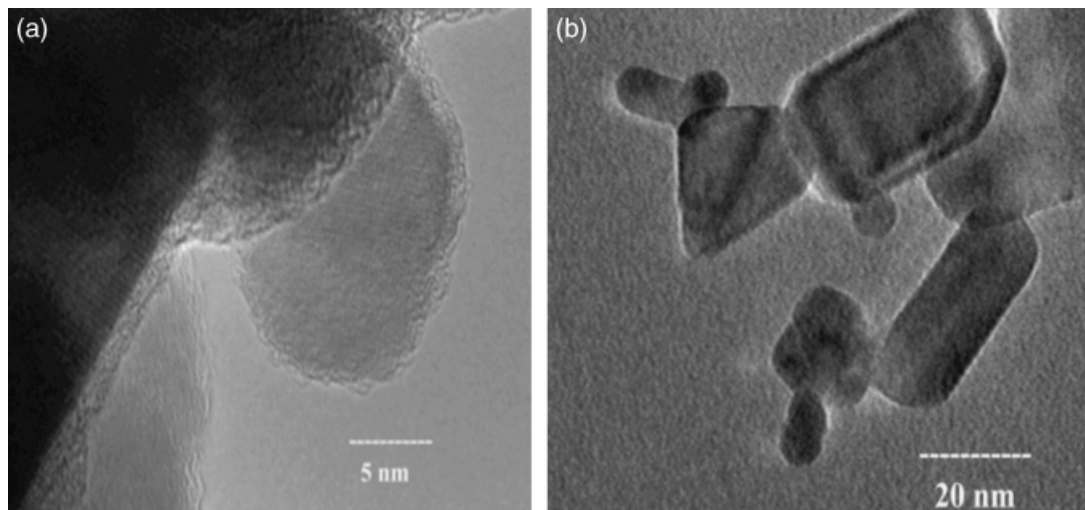


Fig. 12. TEM images of re-shot 30 mol% ZnO in Al_2O_3 .

between spinel and α -alumina should be observed at 30 mol% ZnO composition.

As-produced LF-FSP $(\text{ZnO})_x(\text{Al}_2\text{O}_3)_{1-x}$ ($x = 0.3, 0.5$) powders (3.0 g) were dispersed with 5 mg DARVAN C-N[®] (R.T. Vanderbilt Company Inc., Norwalk, CT) in 100 mL EtOH using a 1.2-cm-diameter 500 W ultrasonic horn (Sonics and Materials 600 VCX, Newtown, CT) at 40% of full power for 12 h. The dispersion was allowed to settle for 24 h. Dispersed nanopowders were mixed with ethanol to a 3.0 wt% ceramic loading, and re-shot in the LF-FSP as described in Section II.

We find that re-shooting produces powders quite different from our anticipated results. The XRDs (Fig. 10) show the phases of the as-produced and re-shot nanopowders at 30 and 50 mol% ZnO compositions. For 50 mol% ZnO samples, phase separation of wurtzite (zincite) and the nonstoichiometric spinel phase (PDF 77-0732) were observed in contrast to the existing thermodynamic data showing phase pure stoichiometric spinel. For 30 mol% ZnO samples, two main phases, wurtzite and spinel (PDF file: 77-0732), with traces of δ -alumina phase form.

Based on the phase diagram,⁴⁴ heating phase pure spinel above approximately 1700°C causes the formation of a liquid phase coincident with the formation of the nonstoichiometric spinel phase (PDF 77-0732). Thus, during LF-FSP reprocessing, this appears to be what happens and on quenching the spinel component retains its nonstoichiometry, whereas the liquid portion is quenched to form wurtzite ZnO. One would therefore expect two different particle morphologies as discussed below but it also may mean that the two particle morphologies observed above arise for similar reasons, the ZnO remains liquid longer than Al^{3+} -doped materials. Since at low Al^{3+} loadings their incorporation leads to an as yet unexplained increase in unit cell dimensions that may arise from formation of interstitials, a better explanation of the above analysis of c/a ratios may be that it is actually averages particles that are pure ZnO and those with higher Al^{3+} doping. At the moment, this remains an open question.

High-resolution SEM and TEM were used to study the morphology of re-shot nanopowders. In Figs. 11 and 12, we observe two different morphologies in the re-processed nanopowders. Comparing with images in previous sections, we expect the cylindrical shape nanoparticles to be zincite and the spherical nanopowders to be nonstoichiometric spinel.

In order to characterize the two different morphologies in the re-shot nanopowders, STEM and XEDS were used. XEDS data (Fig. 14) of four different spots in the STEM image (Fig. 13) were obtained for re-shot 50 mol% ZnO in Al_2O_3 . For cylindrical shapes (spots 2, 3, and 4 in Fig. 13), we observed Zn peaks and no Al peaks in the XEDS [Fig. 14(b)–(d)]. For the spherical particles (spot 1 in Fig. 13), we observe a strong Al peak and a

relatively weak Zn peak in XEDS [Fig. 14(a)] matching the nonstoichiometric spinel in the XRD data. Cu peaks in XEDS come from Cu grid in TEM sample holder.

Thus, our speculation on what happens in the gas phase on re-shooting and perhaps also during initial particle formation seems to be correct. That is, at the flame temperatures used, ZnO remains in the gas phase long enough to produce two different particle morphologies ones with higher Al^{3+} content and particles that are mostly pure ZnO. This then provides a reasonable explanation of the evolution of particle morphology seen in the high ZnO content nanopowders (e.g. >95 mol%). It is important to note that other efforts see well-defined particle compositions, even those using LF-FSP-like approaches.^{44,46} The best explanation is that these studies do not reach the same combustion temperatures used here.

IV. Conclusions

The utility of LF-FSP processing for combinatorial studies of nanopowders along the $(\text{ZnO})_x(\text{Al}_2\text{O}_3)_{1-x}$ tie line was demonstrated focusing on composition regions including Al-doped

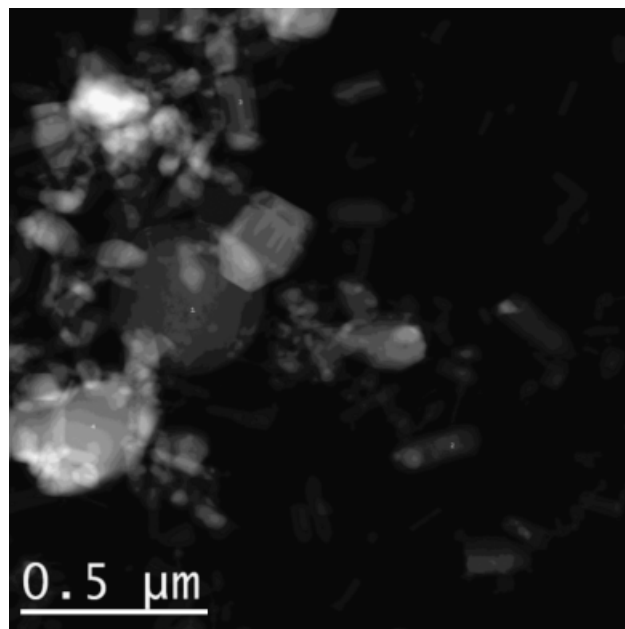


Fig. 13. STEM images of reprocessed 50 mol% ZnO in Al_2O_3 . Note points marked 1–4 which are used for the XED studies in Fig. 14.

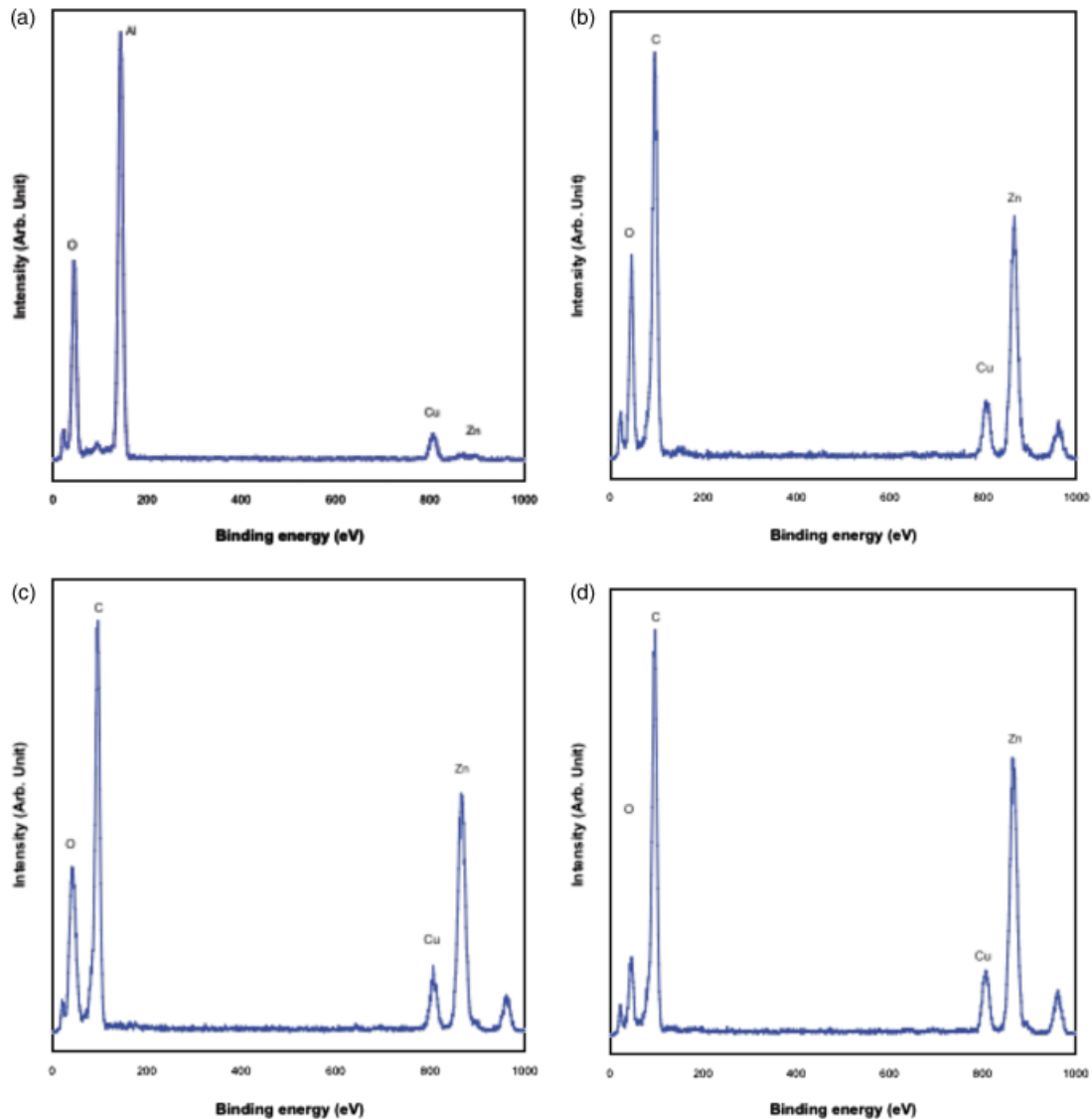


Fig. 14. XEDS of 50 mol% ZnO in Al₂O₃ in spot 1 (a), 2 (b), 3 (c), and 4 (d) from Fig. 13.

ZnO for TCO applications and zinc spinel (ZnAl₂O₄). The resulting data are different from the thermodynamic phase diagram because the resulting nanopowders are kinetic products made by rapid quenching of LF-FSP.

The as-produced powders were characterized in terms of phase, size, composition, and morphology by chemical analysis, FTIR, XRD, SEM, TEM, and TGA-DTA. The XRD data support previous conclusions suggesting that Al³⁺ ions incorporate into interstitial sites of zincite resulting in octahedrally coordinated Al³⁺. At 80 mol% ZnO, small amounts of spinel phase segregate, while the XRD results suggest formation of a single zincite phase at Zn-rich compositions of 99, 95 mol% ZnO. However, the observation of two different particle morphologies in the last two compositions and the results of the re-shooting of phase pure spinel and off-stoichiometry spinel leading to mixed phase nanopowders as a consequence of the low melting temperature of the spinel phase suggest that even in the original powder production gas phase equilibria are of sufficient importance during quenching as to control particle morphologies and the chemical compositions of those particles.

Based on the solubilities of Al₂O₃ in ZnO (up to 20 mol% Al₂O₃) and vice versa, we can suggest an effective operating temperature for LF-FSP processing that ranges between 1700° and 1800°C in ZnO–Al₂O₃ system from the two compositional regions studied. The term “effective” is used because we are not able to estimate the effect(s) of the very small particle sizes and

therefore high surface energies on the solubility of one oxide phase in the other. A more detailed discussion of the thermodynamics of cooling during nanoparticle formation is given elsewhere.⁴⁴

References

- ¹H. Hosono, H. Ohta, M. Orita, K. Ueda, and M. Hirano, “Frontier of Transparent Conductive Oxide Thin Films,” *Vacuum*, **66** [3–4] 419–25 (2002).
- ²I. Hamberg and C. G. Granqvist, “Evaporated Sn-Doped In₂O₃ Films: Basic Optical Properties and Applications to Energy-Efficient Windows,” *J. Appl. Phys.*, **60** [11] R123–59 (1986).
- ³P. P. Edwards, A. Porch, M. O. Jones, D. V. Morgan, and R. M. Perks, “Basic Materials Physics of Transparent Conducting Oxides,” *Dalton Trans.*, [19] 2995–3002 (2004).
- ⁴H. Hono, “Built-in Nanostructures in Transparent Oxides for Novel Photonic and Electronic Functions Materials,” *Int. J. Appl. Ceram. Technol.*, **1** [2] 106–18 (2004).
- ⁵D. S. Ginley and C. Bright, “Transparent Conducting Oxides,” *MRS Bull.*, **25** [8] 15–8 (2000).
- ⁶B. G. Lewis and D. C. Paine, “Applications and Processing of Transparent Conducting Oxides,” *MRS Bull.*, **25** [8] 22–7 (2000).
- ⁷H. Kawazoe, H. Yanagi, K. Ueda, and H. Hosono, “Transparent p-Type Conducting Oxides: Design and Fabrication of p–n Heterojunctions,” *MRS Bull.*, **25** [8] 28–36 (2000).
- ⁸T. Minami, “New n-Type Transparent Conducting Oxides,” *MRS Bull.*, **25** [8] 38–44 (2000).
- ⁹R. G. Gordon, “Criteria for Choosing Transparent Conductors,” *MRS Bull.*, **25** [8] 52–7 (2000).

- ¹⁰T. J. Coutts, D. L. Young, and X. Li, "Characterization of Transparent Conducting Oxides," *MRS Bull.*, **25** [8] 58–65 (2000).
- ¹¹K. Wasa, S. Hayakawa, and T. Hada, "Electrical and Optical Properties of Sputtered *n-p* ZnO-Si Heterojunctions," *Jpn. J. Appl. Phys.*, **10** [12] 1732 (1971).
- ¹²Z. Jin, I. Hamberg, and C. G. Granqvist, "Optical Properties of Sputter-Deposited ZnO:Al Thin Films," *J. Appl. Phys.*, **64** [10] 5117–32 (1988).
- ¹³M. J. Alam and D. C. Cameron, "Preparation and Properties of Transparent Conductive Aluminum-Doped Zinc Oxide Thin Films by Sol-Gel Process," *J. Vac. Sci. Technol. Sect. A*, **19** [4] 1642–6 (2001).
- ¹⁴T. Schuler and M. A. Aegerter, "Optical, Electrical and Structural Properties of Sol Gel ZnO:Al Coatings," *Thin Solid Films*, **351** [1–3] 125–31 (1999).
- ¹⁵S. H. Jeong, J. W. Lee, S. B. Lee, and J. H. Boo, "Deposition of Aluminum-Doped Zinc Oxide Films by RF Magnetron Sputtering and Study of their Structural, Electrical and Optical Properties," *Thin Solid Films*, **435** [1–2] 78–82 (2003).
- ¹⁶T. Suchiya, T. Emoto, and T. Sei, "Preparation and Properties of Transparent Conductive Thin Films by the Sol-Gel Process," *J. Non-Cryst. Solids*, **178**, 327–32 (1994).
- ¹⁷T. Minami, H. Nanto, S. Shooji, and S. Takata, "The Stability of Zinc Oxide Transparent Electrodes Fabricated by R. F. Magnetron Sputtering," *Thin Solid Films*, **111** [2] 167–74 (1984).
- ¹⁸T. Minami, H. Nanto, and S. Takata, "Highly Conductive and Transparent Aluminum Doped Zinc Oxide Thin Films Prepared by RF Magnetron Sputtering," *Jpn. J. Appl. Phys.*, **23** [5] L280–2 (1984).
- ¹⁹C. R. Bickmore, K. F. Waldner, D. R. Treadwell, and R. M. Laine, "Ultrafine Spinel Powders by Flame Spray Pyrolysis of a Magnesium Aluminum Double Alkoxide," *J. Am. Ceram. Soc.*, **79** [5] 1419–23 (1996).
- ²⁰C. R. Bickmore, K. F. Waldner, R. Baranwal, T. Hinklin, D. R. Treadwell, and R. M. Laine, "Ultrafine Titania by Flame Spray Pyrolysis of a Titanatran Complex: Part I," *J. Eur. Ceram. Soc.*, **18** [4] 287–97 (1998).
- ²¹A. C. Sutorik, S. S. Neo, T. Hinklin, R. Baranwal, D. R. Treadwell, R. Narayanan, and R. M. Laine, "Synthesis of Ultrafine β -Alumina Powders Via Flame Spray Pyrolysis of Polymeric Precursors," *J. Am. Ceram. Soc.*, **81** [6] 1477–86 (1998).
- ²²T. Hinklin, B. Toury, C. Gervais, F. Babonneau, J. J. Gislason, R. W. Morton, and R. M. Laine, "Liquid-Feed Flame Spray Pyrolytic Synthesis of Nanoalumina Powders," *Chem. Mater.*, **16** [1] 21–30 (2004).
- ²³R. M. Laine, R. Baranwal, T. Hinklin, D. Treadwell, A. Sutorik, C. R. Bickmore, K. Waldner, and S. S. Neo, "Making Nanosized Oxide Powders from Precursors by Flame Spray Pyrolysis"; pp. 17–24 in *Novel Synthetic and Processing Routes to Ceramics. Key Engineering Materials*, Vols. 159–160, Edited by K. Uematsu, and H. Otsuka. K. Trans Tech Publ. Ltd., Switzerland, 1998.
- ²⁴R. Baranwal, M. P. Villar, R. Garcia, and R. M. Laine, "Synthesis, Characterization, and Sintering Behavior of Nano-Mullite Powder and Powder Compacts," *J. Am. Ceram. Soc.*, **84** [5] 951–61 (2001).
- ²⁵G. Williams, S. C. Rand, T. Hinklin, and R. M. Laine, "Laser Action in Strongly Scattering Rare-Earth-Doped Dielectric Nanophosphors," *Phys. Rev. A*, **65** [1] 013807–6 (2002).
- ²⁶S. Kim, J. J. Gislason, R. W. Morton, X. Pan, H. Sun, and R. M. Laine, "Liquid-Feed Flame Spray Pyrolysis of Nanopowders in the Alumina-Titania System," *Chem. Mater.*, **16** [12] 2336–43 (2004).
- ²⁷J. Marchal, T. Hinklin, R. Baranwal, T. Johns, and R. M. Laine, "Yttrium Aluminum Garnet Nanopowders by Flame Spray Pyrolysis," *Chem. Mater.*, **16** [5] 822–31 (2004).
- ²⁸R. M. Laine, J. Marchal, H. J. Sun, and X. Q. Pan, "A New $Y_3Al_5O_{12}$ Phase Produced by Liquid-Feed Flame Spray Pyrolysis (LF-FSP)," *Adv. Mater.*, **17** [7] 830–3 (2005).
- ²⁹J. A. Azurdia, J. C. Marchal, P. Shea, H. Sun, X. Q. Pan, and R. M. Laine, "Liquid-Feed Flame Spray Pyrolysis (LF-FSP) as a Method of Producing Mixed-Metal Oxide Nanopowders of Potential Interest as Catalytic Materials. Nanopowders Along the NiO–Al₂O₃ Tie-Line Including (NiO)_{0.22}(Al₂O₃)_{0.78}, a New Inverse Spinel Composition," *Chem. Mater.*, **18** [9] 731–9 (2006).
- ³⁰J. A. Azurdia, J. C. Marchal, and R. M. Laine, "Combinatorial Processing of Mixed-Metal Oxide Nanopowders Along the Co₃O₄–Al₂O₃ Tie Line Using Liquid-Feed Flame Spray Pyrolysis (LF-FSP)," *J. Am. Ceram. Soc.*, **89** [9] 2749–56 (2006).
- ³¹T. R. Hinklin and R. M. Laine, "Synthesis of Metastable Phases in the Magnesium Spinel–Alumina System," *Chem. Mater.*, **20** [2] 553–8 (2008).
- ³²M. Kim and R. M. Laine, "Combinatorial Processing of Mixed-Metal Oxide Nanopowders Along the ZrO₂–Al₂O₃ Tie Line Using Liquid-Feed Flame Spray Pyrolysis (LF-FSP)," *J. Ceram. Process. Res.*, **8** [2] 129–36 (2007).
- ³³M. Kim, T. R. Hinklin, and R. M. Laine, "Core-Shell Nanostructured Nanopowders Along (CeO_x)_x(Al₂O₃)_{1-x} Tie-Line by Liquid-Feed Flame Spray Pyrolysis (LF-FSP)," *Chem. Mater.*, **20** [16] 5154–62 (2008).
- ³⁴T. T. Kodas and M. J. Hampden-Smith, *Aerosol Processing of Materials*. Wiley-VCH, New York, 1999.
- ³⁵M. Winterer, *Nanocrystalline Ceramics, Synthesis and Structure*. Springer, Lausanne, 2002.
- ³⁶F. E. Luborsky, "Highly Coercive Materials, Development of Elongated Particle Magnets," *J. Appl. Phys.*, **32**, S171–9 (1961).
- ³⁷B. L. Cushing, V. L. Kolesnichenko, and C. J. O'Connor, "Recent Advances in the Liquid-Phase Syntheses of Inorganic Nanoparticles," *Chem. Rev.*, **104**, 3893–946 (2004).
- ³⁸M. T. Swihart, "Vapor-Phase Synthesis of Nanoparticles," *Curr. Opin. Coll. Inter. Sci.*, **8**, 127–33 (2003).
- ³⁹F. E. Kruijs, H. Fissan, and A. Peled, "Synthesis of Nanoparticles in the Gas Phase for Electronic, Optical and Magnetic Applications—A Review," *J. Aerosol Sci.*, **29**, 511–35 (2004).
- ⁴⁰L. Madler, "Liquid-Fed Aerosol Reactors for One-Step Synthesis of Nano-Structured Particles," *Kona*, **22**, 107–20 (2004).
- ⁴¹R. Strobel and S. E. Pratsinis, "Flame Aerosol Synthesis of Smart Nanostructured Materials," *J. Mater. Chem.*, **17**, 4743–56 (2007).
- ⁴²R. M. Laine, "Liquid-Flame Spray Pyrolysis (LF-FSP) in the Synthesis of Single and Mixed-Metal Oxide Nanopowders"; in *Ceramics Science and Technology*, Vol. 3, Edited by R. Riedel, and I.-W. Chen. Wiley VCH Weinheim, in press.
- ⁴³E. Arca, K. Fleischer, and I. V. Shvets, "Influence of the Precursors and Chemical Composition of the Solution on the Properties of ZnO Thin Films Grown by Spray Pyrolysis," *J. Phys. Chem. C*, **113**, 21074–81 (2009).
- ⁴⁴J. U. Brehma, M. Winterer, and H. Hahn, "Synthesis and Local Structure of Doped Nanocrystalline Zinc Oxides," *J. Appl. Phys.*, **100**, 064311, 9pp (2006).
- ⁴⁵S. Suwanboon, P. Amornpitoksuk, A. Haidoux, and J. C. Tedenac, "Structural and Optical Properties of Undoped and Aluminium Doped Zinc Oxide Nanoparticles Via Precipitation Method at Low Temperature," *J. Alloys Compd.*, **462**, 335–9 (2008).
- ⁴⁶T. Ogi, D. Hidayat, F. Iskandar, A. Purwanto, and K. Okuyama, "Direct Synthesis of Highly Crystalline Transparent Conducting Oxide Nanoparticles by Low Pressure Spray Pyrolysis," *Adv. Powder Technol.*, **20**, 203–9 (2009).
- ⁴⁷B. Houg and C.-J. Huang, "Structure and Properties of Ag Embedded Aluminum Doped ZnO Nanocomposite Thin Films Prepared Through a Sol-Gel Process," *Surf. Coat. Technol.*, **201**, 3188–92 (2006).
- ⁴⁸Z. Ben Ayadi, L. El Mir, K. Djessas, and S. Alaya, "The Properties of Aluminum-Doped Zinc Oxide Thin Films Prepared by rf-Magnetron Sputtering from Nanopowder Targets," *Mater. Sci. Eng. C*, **28**, 613–7 (2008).
- ⁴⁹S. Cho, S.-H. Jung, J.-W. Jang, E. Oh, and K.-H. Lee, "Simultaneous Synthesis of Al-Doped ZnO Nanoneedles and Zinc, Aluminum Hydroxides through Use of a Seed Layer," *Cryst. Growth Design*, **8**, 4553–8 (2008).
- ⁵⁰X. L. Cheng, H. Zhao, L. H. Huo, S. Gao, and J. G. Zhao, "ZnO Nanoparticulate Thin Film: Preparation, Characterization and Gas-Sensing Property," *Sensors Actuators B*, **102**, 248–52 (2004).
- ⁵¹J. B. McPeak and K. M. Baxter, "Microreactor for High-Yield Chemical Bath Deposition of Semiconductor Nanowires: ZnO Nanowire Case Study," *Ind. Eng. Chem. Res.*, **48**, 5954–61 (2009).
- ⁵²J.-S. Na, Q. Peng, G. Scarel, and G. N. Parsons, "Role of Gas Doping Sequence in Surface Reactions and Dopant Incorporation During Atomic Layer Deposition of Al-Doped ZnO," *Chem. Mater.*, **21**, 5585–93 (2009).
- ⁵³S. Hartner, M. Ali, C. Schulz, H. Winterer, and M. Wiggers, "Electrical Properties of Aluminum-Doped Zinc Oxide (AZO) Nanoparticles Synthesized by Chemical Vapor Synthesis," *Nanotechnology*, **20**, 445701 (2009).
- ⁵⁴A. B. F. Martinson, J. W. Elam, J. T. Hupp, and M. J. Pellin, "ZnO Nanotube Based Dye-Sensitized Solar Cells," *Nano Lett.*, **7**, 2183–7 (2007).
- ⁵⁵T. Strachowski, E. Grzanka, W. Lojowski, A. Presz, M. Godlewski, S. Yatsunenok, H. Matysiak, R. R. Piticescu, and C. J. Monty, "Morphology and Luminescence Properties of Zinc Oxide Nanopowders Doped with Aluminum Ions Obtained by Hydrothermal and Vapor Condensation Methods," *J. Appl. Phys.*, **102**, 073513 (2007).
- ⁵⁶J. D. Merchant and M. Cocivera, "Preparation and Doping of Zinc Oxide Using Spray Pyrolysis," *Chem. Mater.*, **7**, 1742–9 (1995).
- ⁵⁷T. Masaki, S.-J. Kim, H. Watanabe, K. Miyamoto, M. Ohno, and K.-H. Kim, "Synthesis of Nano-Sized ZnO Powders Prepared by Precursor Process," *J. Ceram. Process. Res.*, **4**, 135–9 (2003).
- ⁵⁸R. R. Piticescu, R. M. Piticescu, and C. J. Monty, "Synthesis of Al-Doped ZnO Nanomaterials with Controlled Luminescence," *J. Eur. Ceram. Soc.*, **26**, 2979–83 (2006).
- ⁵⁹R. M. Laine, J. C. Marchal, H. P. Sun, and X. Q. Pan, "Nano- α -Al₂O₃ by Liquid-Feed Flame Spray Pyrolysis (LF-FSP) of Nano-Transition Aluminas," *Nat. Mater.*, **5** [9] 710–2 (2006).
- ⁶⁰E. N. Bunting, "Phase Equilibria in the System SiO₂–ZnO–Al₂O₃," *Bur. Stand. J. Res.*, **8**, 279–9 (1932).
- ⁶¹R. Hansson, P. C. Hayes, and E. Jak, "Experimental Study of Phase Equilibria in the Al–Fe–Zn–O System in Air," *Metall. Mater. Trans. B*, **35** [4] 633–42 (2004).
- ⁶²H. Kim, A. Pique, J. S. Horwitz, H. Murata, Z. H. Kafafi, C. M. Gilmore, and D. B. Chrisey, "Effect of Aluminum Doping on Zinc Oxide Thin Films Grown by Pulsed Laser Deposition for Organic Light-Emitting Devices," *Thin Solid Films*, **377–378** [1] 798–802 (2000).
- ⁶³H. Cao, C. Sun, Z. Pei, A. Wang, L. Wen, R. Hong, and X. Jiang, "Properties of Transparent Conducting ZnO:Al Oxide Thin Films and their Application for Molecular Organic Light-Emitting Diodes," *J. Mater. Sci.: Mater. Elect.*, **15** [3] 169–74 (2004).
- ⁶⁴R. Hansson, P. C. Hayes, and E. Jak, "Experimental Study of Phase Equilibria in the Al–Fe–Zn–O System in Air," *Metall. Mater. Trans. B*, **35** [4] 633–42 (2004).
- ⁶⁵X. Liu and R. E. Truitt, "DRFT-IR Studies of the Surface of γ -Alumina," *J. Am. Chem. Soc.*, **119** [41] 9856–60 (1997).
- ⁶⁶J. B. Peri, "Infrared and Gravimetric Study of the Structure Hydration of γ -Alumina," *J. Phys. Chem.*, **69** [1] 211–9 (1965).
- ⁶⁷S. Shen, K. Hidayat, L. Yu, and S. Kawi, "Simple Hydrothermal Synthesis of Nanostructured and Nanorod Zn–Al Complex Oxides as Novel Nanocatalysts," *Adv. Mater.*, **16** [6] 541–5 (2004).
- ⁶⁸A. Adak, A. Pathak, and P. Pramanik, "Characterization of ZnAl₂O₄ Nanocrystals Prepared by the Polyvinyl Alcohol Evaporation Route," *J. Mater. Sci. Lett.*, **17** [7] 559–61 (1998).
- ⁶⁹S. V. Tsybulya, L. P. Solov'eva, L. M. Plyasova, and O. P. Krivoruchko, "Complete-Profile Analysis Applied to Nonstoichiometric Spinel," *J. Struct. Chem.*, **32** [1] 386–8 (1991).
- ⁷⁰A. N. Tsvignunov, V. G. Khotin, A. S. Krasikov, and B. S. Svetlov, "Shock-Wave Synthesis of Nonstoichiometric Aluminizing Spinel and Gahnite," *Glass Ceram.*, **58** [9–10] 353–5 (2002). □